

The Vacancy-Induced Electronic Structure of the SrTiO_{3-δ} Surface

Seyoung Cook, Maxwell T. Dylla, Richard A. Rosenberg, Zachary R. Mansley, G. Jeffrey Snyder, Laurence D. Marks, and Dillon D. Fong*

The emergence of a 2D electron gas (2DEG) on the (001) surface of oxygen-deficient strontium titanate (SrTiO_{3-δ}) is investigated. Using in situ soft X-ray spectroscopy and effective mass modeling, a series of quantitative band diagrams are developed to describe the evolution of near-surface and bulk carrier concentrations, downward band bending, and Fermi level along a lateral gradient of oxygen vacancies formed on SrTiO_{3-δ} by direct-current resistive heating under ultrahigh vacuum conditions. Electrons are accumulated over a 3 nm region near the surface, confined within a potential well with saturated 300 meV downward band bending. The relation between Fermi levels and carrier concentrations near the surface suggests the density of states near the surface is much lower than the bulk density of states, which is consistent with the quantum-confined subbands of a 2DEG. The quantitative relationship between the surface and bulk electronic structures developed in this work provides a guide for precise engineering of the oxygen-vacancy-induced 2DEG in SrTiO₃.

1. Introduction

Correlated electrons at the interfaces of transition metal oxides give rise to exotic physical properties that can be combined with the intrinsic functionalities of oxides for future electronic devices.^[1–3] Strontium titanate (SrTiO₃ or STO) has long been the preferred substrate material for the growth of epitaxial oxide thin films, and has emerged as a key material for oxide-based electronics with the discovery of high-mobility 2D electron gases (2DEGs) at its interface with crystalline LaAlO₃ (LAO)^[4] and other oxides.^[5–9] In particular, the 2DEG at the LAO/STO

interface was shown to be tunable by an electric-field effect,^[10,11] leading to the discovery of gate-tunable exotic properties such as superconductivity,^[11–14] magnetism,^[15] and Rashba interaction,^[16–18] which can be exploited in novel electronic and spintronic devices.^[19]

The intriguing conductivity arising between LAO and STO—both of which are wide band gap insulators with band gaps of 5.6 and 3.2 eV, respectively—was initially explained by the polar catastrophe model.^[4,20] According to this model, a charge of 0.5 e⁻ per square STO lattice parameter is transferred from the LAO surface to the STO side of the interface to prevent the electrical potential from diverging due to the polar stacking of LaO⁺ and AlO₂⁻ layers. **Figure 1a** illustrates this behavior, in which a downward bending of STO bands near the

interface creates a narrow potential well that accommodates and confines the transferred charge at the interface, forming the 2DEG. However, numerous reports have proposed alternative explanations for the origin of the 2DEG, including charge doping by oxygen vacancies and cation intermixing.^[21–26]

Interestingly, angle-resolved photoemission spectroscopy (ARPES) studies showed that a similar 2DEG can be stabilized on the bare surface of STO (001) cleaved under ultrahigh vacuum (UHV) conditions following ultraviolet (UV)-light irradiation.^[27–29] The 2DEG in this case is an electron accumulation layer that screens the positively charged oxygen vacancy defects (V_O²⁺ or V_O⁻ in Kröger–Vink notation) formed near the surface. The positively charged oxygen vacancies donate charge (e⁻) while also inducing downward band bending at the STO surface, providing a confining potential well for the doped electrons. This is illustrated schematically in **Figure 1b** and also in **Figure 1c**, where the 2DEG is shown to form from Ti 3d t_{2g}-derived quantized states (subbands).

Recent studies have employed a variety of techniques to generate a 2DEG on the STO surface, also based on oxygen vacancy formation, including in situ sputtering,^[30] vacuum annealing,^[31,32] and metal deposition.^[33] However, the quantitative relationship between the surface and bulk electronic structures remains unclear in some of these studies, especially given that n-type conducting (Nb-doped) STO substrates are often used to permit ARPES measurements.^[30–32] In these

Dr. S. Cook, Dr. D. D. Fong
Materials Science Division
Argonne National Laboratory
Argonne, IL 60439, USA
E-mail: fong@anl.gov

Dr. S. Cook, M. T. Dylla, Z. R. Mansley, Prof. G. J. Snyder, Prof. L. D. Marks
Department of Materials Science and Engineering
Northwestern University
Evanston, IL 60208, USA

Dr. R. A. Rosenberg
X-ray Science Division
Argonne National Laboratory
Argonne, IL 60439, USA

 The ORCID identification number(s) for the author(s) of this article can be found under <https://doi.org/10.1002/aelm.201800460>.

DOI: 10.1002/aelm.201800460

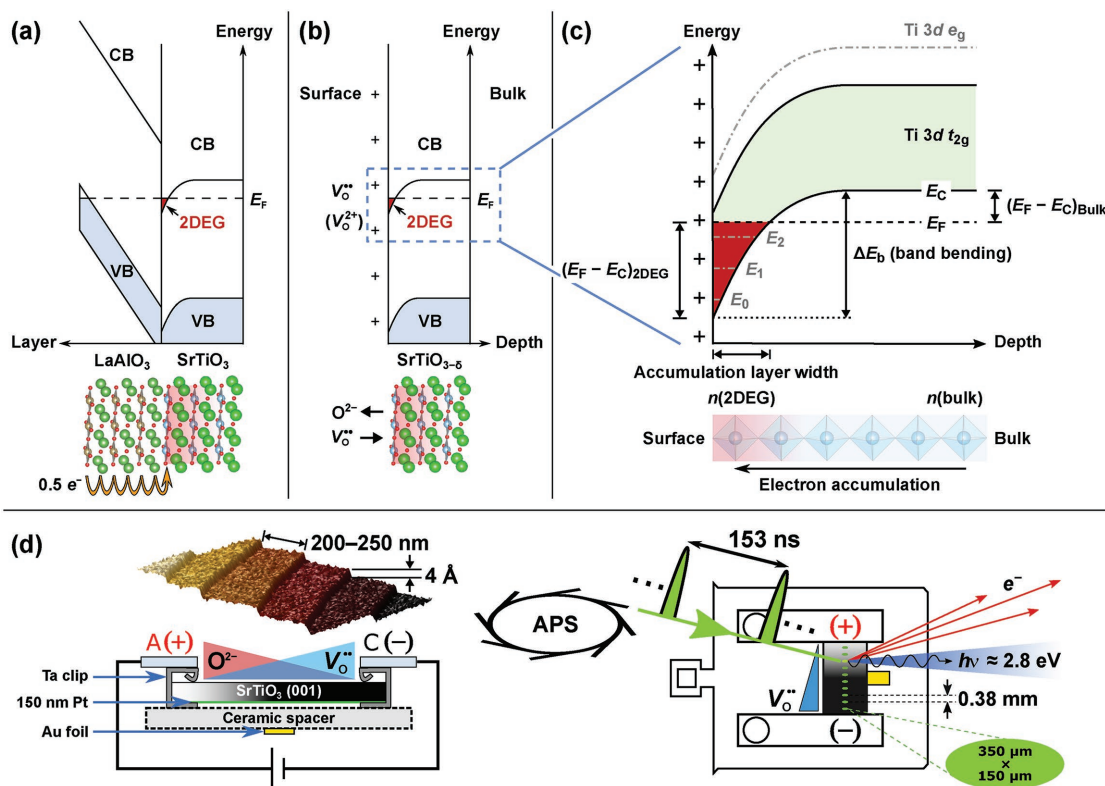


Figure 1. Role of band bending in the formation of 2DEGs in SrTiO₃ (STO)-based systems and the experimental approach used to systematically probe 2DEG formation in reduced SrTiO_{3-δ}. a) Schematic band diagram of 2DEG formed at the LaAlO₃/SrTiO₃ interface according to the polar catastrophe model. b) Schematic band diagram of 2DEG formed near the surface of SrTiO_{3-δ} due to the dual role of oxygen vacancies (V_O^{••}) in providing carriers and a positive surface potential. c) Details of the band diagram near the conduction band edge including the formation of Ti 3d-derived subbands of t_{2g} character (gray). The carrier concentrations near the surface (n(2DEG)) and in the bulk (n(bulk)) are related by band bending (ΔE_b) and Fermi level (E_F - E_C). d) Schematic illustrations of the DC-resistive heater setup and the X-ray spectroscopy measurements performed over a gradient of oxygen vacancies formed on a STO (001) single crystal prepared with a TiO₂-terminated surface (inset tapping-mode atomic force microscopy image). Application of a DC bias under UHV conditions heats the sample between 700 and 800 °C and drives O²⁻ anions from the cathode (-) toward the anode (+), producing a gradient of oxygen vacancies. The varying vacancy-induced electronic structures and doped electron concentrations are probed using soft X-ray spectroscopy.

systems, the 2DEG electron density $n(2DEG)$, the bulk carrier concentration $n(bulk)$, and the amount of band bending ΔE_b are linked via the Fermi level E_F (here referenced with respect to the conduction band minimum, E_C), which together define the depth of the potential well near the surface and the width of the accumulation layer, as depicted in Figure 1c. In order to determine this, one must distinguish and quantify the electrons accumulated near the surface versus those doped in the bulk of the STO crystal.

To overcome these challenges, we take advantage of the blue luminescence property of electron-doped STO, which exhibits a broad blue luminescence band around 2.8 eV at room temperature due to the radiative recombination of electrons and holes.^[34–36] The lifetime of the blue luminescence varies with the doped electron concentration when the dynamics of the photocarriers are dominated by the Auger recombination process.^[37] In this work, X-ray excited optical luminescence (XEOL) is used to measure the spatially-dependent lifetimes of the blue luminescence components associated with the 2DEG near the surface and doped electrons in the bulk, allowing us to distinguish and quantify the two electron populations.

Here, we report a detailed study of the evolving electronic structure of STO describing the formation of a 2DEG on the STO (001) surface created by a simple vacuum annealing process. Direct-current (DC) resistive heating was applied along a TiO₂-terminated STO (001) single crystal under UHV conditions to create a gradient of oxygen vacancies along the length of the sample. Using in situ soft X-ray spectroscopy and effective mass modeling, we develop a series of quantitative band diagrams describing the evolution of electronic structure along the oxygen vacancy gradient, including the near-surface and bulk carrier concentrations, downward band bending, and Fermi level. We find that electrons accumulate over a 3 nm region near the surface within a potential well characterized by downward band bending that saturates at 300 meV. We show that the electrons near the surface are characterized by a much lower density of states compared to the bulk electrons, which is attributed to a reconstructed density of states derived from quantum-confined subbands consistent with a 2DEG. Our quantitative results inform the design of oxide interfaces with optimal electronic structures, through defect engineering of the STO substrate via vacuum annealing.

2. Results and Discussion

2.1. Tracking the Oxygen Vacancy Formation Using Blue Luminescence

A TiO₂-terminated STO (001) single crystal was subjected to DC-resistive heating under UHV conditions, as schematically shown in Figure 1d. The DC field heats a Pt thin film deposited on the backside of the STO single crystal, causing migration of O²⁻ ions from the cathode to the anode and leaving behind a lateral gradient of oxygen vacancies (V_O) across the sample. Following annealing, soft X-ray spectroscopy measurements were performed at room temperature along the length of the sample using focused X-ray beams to characterize the evolving electronic structures along the oxygen vacancy gradient.

Formation of the vacancy gradient was tracked by monitoring the color change during the heating process and measuring the evolution of the blue luminescence after cooling. As shown in Figure 2a, annealing for 40 min between 700–800 °C leads to an apparent spatial color gradation, with the darker region resulting from oxygen deficiencies reaching about half the sample length. XEOL spectra taken at room temperature,

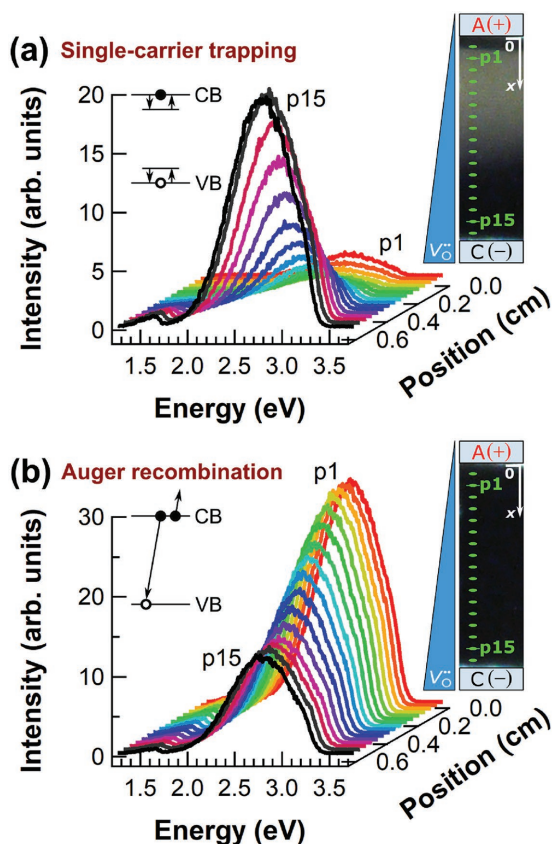


Figure 2. Evolution of the room-temperature blue luminescence intensities along the oxygen vacancy gradient formed after DC resistive heating. XEOL spectra and sample photo taken a) after annealing at 700–800 °C for 40 min and b) after annealing at the same temperatures for an additional 1 h. Inset diagrams illustrate the nonradiative recombination processes which dominate the photocarrier dynamics at each annealing stage. Black dots denote electrons and white circles denote holes in the conduction band (CB) and valence band (VB), respectively.

also presented in Figure 2a, showed the emergence of blue luminescence peaked at 2.73 eV. The luminescence intensity correlates with the visible color gradation, increasing from the less reduced region (position p1) to the more reduced region (position p15). This is due to the nonradiative single-carrier trapping recombination process that dominates photocarrier dynamics in the low-doping limit^[37] (inset of Figure 2a).

Annealing for an additional 1 h between 700 and 800 °C results in a complete color change over the length of the crystal. This time, however, the room-temperature blue luminescence intensity is stronger in the less reduced region and weaker in the more reduced region, as shown in Figure 2b. The decrease in blue luminescence intensity is due to shortening of the lifetimes as electron doping increases above a critical concentration, at which the Auger recombination process dominates the photocarrier dynamics^[37,38] (inset of Figure 2b). All subsequent measurements reported in this work were performed on this sample.

As reported in previous photoluminescence works,^[37,39] the room-temperature blue luminescence of STO stems from the two-carrier radiative recombination of electrons and holes. In electron-doped STO where the photoexcited carrier density (n) is far below the doped carrier density (N_e), Auger recombination of photoexcited holes and doped electrons is dominant, and the recombination of photoexcited electrons and holes is negligible. In this regime, the rate equation for the photocarrier dynamics and the intensity of the blue luminescence are described the following equations

$$\frac{dn}{dt} = -An - CN_e^2n \quad (N_e \gg n) \quad (1)$$

$$I(t) \propto BN_e n(t) \quad (2)$$

Here, $I(t)$ and $n(t)$ are the luminescence intensity and the photocarrier density, respectively. A is the single-carrier trapping rate, B is the two-carrier radiative recombination coefficient, and C is the three-carrier Auger recombination rate. According to Equations (1) and (2), blue luminescence is expected to exhibit exponential decay, where the lifetime $\tau = (A + CN_e^2)^{-1}$ is determined by the doped electron concentration N_e . Thus, in the limit where $N_e > \sqrt{A/C}$, the Auger recombination process dominates the photocarrier dynamics, and the doped electron concentration can be determined for a given lifetime if the two recombination coefficients A and C are known.

As shown in Figure 3a, the XEOL decay curves monitored at the 2.73 eV blue luminescence emission energy exhibit decreasing lifetimes as the doped electron concentration increases from position p1 to position p15 due to increasing oxygen vacancy concentration. The luminescence decay curves are well described by a double exponential function convolved with the instrument response function (IRF) fitted using a least-squares minimization algorithm, indicating that there are two components to the observed blue luminescence

$$I(t) = \alpha_1 e^{-\frac{t}{\tau_1}} + \alpha_2 e^{-\frac{t}{\tau_2}} \quad (3)$$

with lifetimes τ_n and pre-exponential factors α_n . The sum of the pre-exponential factors was constrained to be one in order

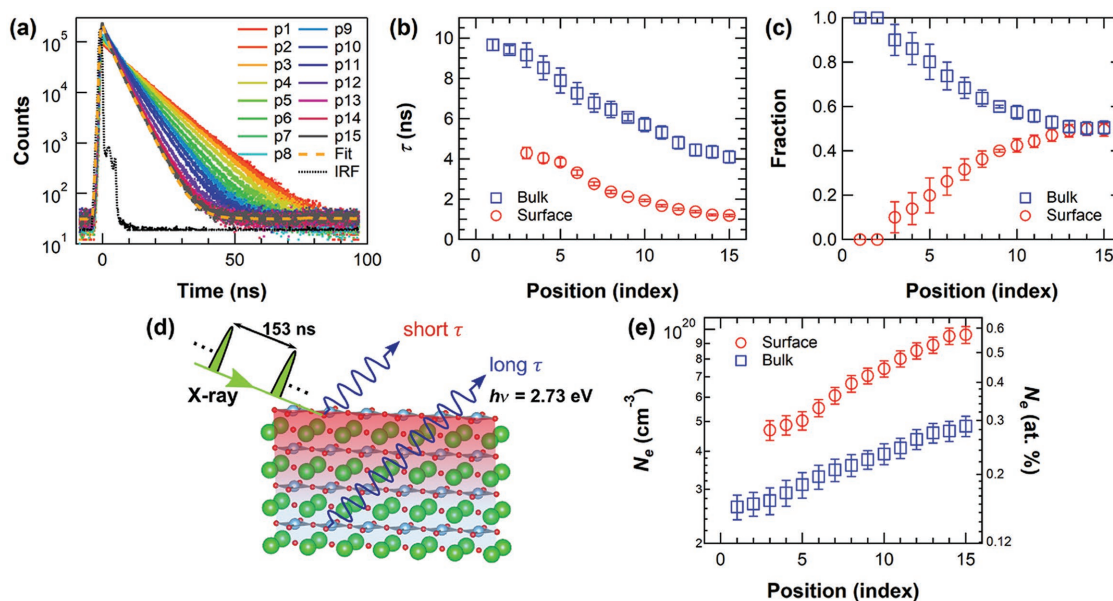


Figure 3. Evolving blue luminescence dynamics along the oxygen vacancy (V_O) gradient and quantification of the doped electron concentrations in the near-surface and bulk regions. a) Post-anneal XEOL decay curves monitored at the 2.73 eV blue luminescence emission energy along the V_O gradient. The instrument response function (IRF) of the measurement setup and a double exponential fit convolved with the IRF for the decay curve corresponding to a reduced region (position p15) are also shown. The IRF presented here is scaled in the y-axis. b) Lifetimes and c) pre-exponential factors obtained from the biexponential fits to the blue luminescence decay curves. d) Illustration of the spatial origins of the two blue luminescence decay components; from electrons doped near the surface and in the bulk of the STO crystal. e) Doped electron concentrations profiles along the V_O gradient for the near-surface and bulk regions corresponding to the fast and slow blue luminescence decay components, respectively. All uncertainties are given by standard deviations.

to represent fractions of blue luminescence with different lifetimes. The fit results for position p15, along with the IRF, are shown in Figure 3a. Similar fitting was performed for the rest of the decay curves (Section SI of the Supporting Information). In Figure 3b,c, we present the lifetimes and pre-exponential factors of the two exponential decay components obtained from fitting the blue luminescence decay curves. The two components can be clearly distinguished into fast and slow components, which we tentatively assign to the surface and bulk contributions, respectively. These assignments physically correspond to the contributions to the blue luminescence from electrons accumulated over a narrow region near the surface and electrons distributed homogeneously in the bulk, as illustrated in Figure 3d and elaborated further below. The lifetimes of the fast surface component are about 1.5–2 times shorter than those of the slow bulk component, but they follow a similar decreasing trend with increasing doped electron concentrations across the oxygen vacancy gradient. While the fraction of the fast surface component is negligible in the less reduced regions (positions p1 and p2), it grows to 50% of the total luminescence decay along the length of the oxygen vacancy gradient.

The lifetimes of the slow and fast components allow determination of the doped electron concentrations near the surface and in the bulk, respectively. The single-carrier trapping coefficient A and the Auger recombination coefficient C were first determined from the lifetimes of blue luminescence decay curves of as-received, epipolished 0.1 and 0.2 at% Nb-doped SrTiO_3 (Nb:STO) (001) substrates, as detailed in Section SII of the Supporting Information. We obtain $A = (4.4 \pm 0.2) \times 10^7 \text{ s}^{-1}$ and $C = (8.6 \pm 0.9) \times 10^{-32} \text{ cm}^6 \text{ s}^{-1}$. These values agree closely

with the values obtained from previous photoluminescence measurements on electron-doped SrTiO_3 .^[37,39] Figure 3e shows the doped electron concentrations associated with the slow bulk and fast surface components calculated using the values of A and C obtained from our analysis. These results indicate, starting from position p3 in our sample, the emergence of a near-surface region with electron concentrations that are 1.5–2 times larger than the bulk, with N_e reaching up to $1 \times 10^{20} \text{ cm}^{-3}$ (0.6 at%) at position p15.

2.2. Electron Accumulation from Band Bending

We now rationalize the observed enhanced electron doping in the near-surface region as a 2DEG confined within a few unit cells near the surface of STO. To this end, we considered band bending near the surface, which would form the potential well necessary for the 2DEG. Direct evidence of band bending was provided by chemical shifts measured in the core-level X-ray photoelectron spectroscopy (XPS) spectra with different probe depths along the lateral vacancy gradient, as illustrated in Figure 4a. In measuring the O 1s, Ti 2p, and Sr 3d core-levels with a photon energy of 1000 eV, the probe depths are within 3 and 8 nm at emission angles of $\theta = 30^\circ$ and $\theta = 80^\circ$, respectively. At the more surface-sensitive condition ($\theta = 30^\circ$), all core-level peaks exhibit shifts towards higher binding energies (downward band bending) with increasing oxygen vacancy concentration (Figure S3a, Supporting Information). This indicates that within ≈ 3 nm of the STO surface, the degree of downward band bending increases monotonically along the length of the

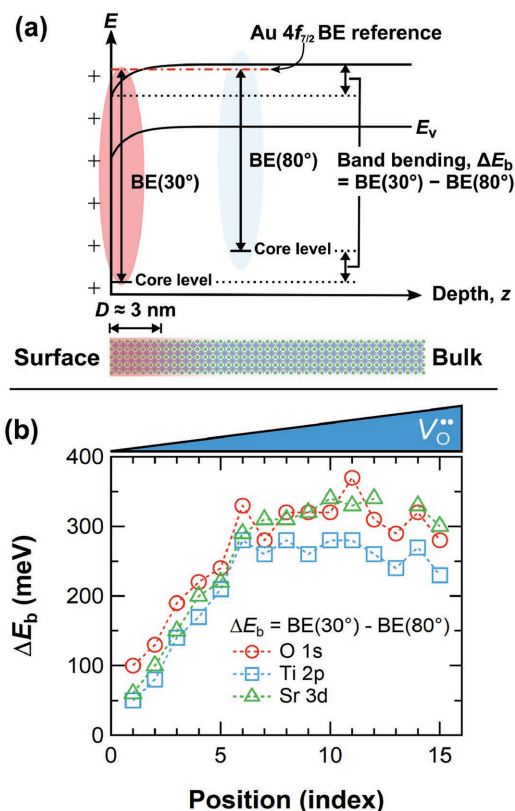


Figure 4. Downward band bending near the surface deduced from core-level XPS peak shifts. a) Schematic band diagram illustrating the depth-dependence of XPS measurements. Binding energies (BEs) of core-level peaks measured at emission angle $\theta = 30^\circ$ and photon energy $h\nu = 1000$ eV are relatively surface sensitive with 95% photoelectron probe depths of 1.7, 1.9, and 2.7 nm for the O 1s, Ti 2p, and Sr 3d core-level peaks, respectively. At an emission angle $\theta = 80^\circ$, the measurements become more bulk sensitive with probe depths of 5.1, 5.7, and 8.0 nm for the O 1s, Ti 2p, and Sr 3d core-level peaks, respectively. All BEs are referenced to Au $4f_{7/2}$ at 84.0 eV. b) Band bending ΔE_b near the surface estimated from the core-level binding energies $BE(30^\circ)$ and $BE(80^\circ)$ measured at 30° and 80° emission angles, respectively.

oxygen vacancy gradient. On the other hand, with regard to XPS spectra taken under more bulk-sensitive condition ($\theta = 80^\circ$), the binding energies along the oxygen vacancy gradient no longer monotonically increase (Figure S3b, Supporting Information). The difference in binding energies between the two probe depths, ΔE_b , gives an estimate of the band bending at each position along the oxygen vacancy gradient, and is shown in Figure 4b. The amount of surface band bending increases along the length of the oxygen vacancy gradient until saturating at ≈ 300 meV by position p6.

2.3. Band-Diagram Descriptions of Oxygen-Vacancy-Induced Electronic Structures

The data above enable construction of quantitative band diagrams describing the depth-dependent electronic structure of the reduced STO sample. First, we present the band diagram in Figure 5a that provides general information, including states

within the band gap. The first set of states we detect in the gap were observed from a combination of XPS, X-ray absorption spectroscopy (XAS), and resonant photoemission spectroscopy (RESPES) measurements, as discussed in Section SIV of the Supporting Information. These in-gap states (IGS) arise from surface oxygen vacancies and TiO_x surface phases formed in the DC-resistive heating process (Figures S4 and S6, Supporting Information). The clearest spectroscopic signatures we detect are broad Ti 3d states peaked ≈ 0.93 eV below the Fermi level (E_F) in the RESPES of the valence band region (Figure S5, Supporting Information), which have been associated with surface oxygen vacancies in the literature.^[40] The second state we detect from XEOL spectra is the deep-level trap state^[36] located 2.73 eV above the valence band maximum, which facilitates the radiative recombination of electrons and holes for blue luminescence. In the subsequent discussion, we explain the two carrier concentrations in terms of the near-surface band-bending XPS results.

The position of the Fermi level with respect to the bulk conduction band minimum was determined by an effective mass model (Section SV of the Supporting Information). This technique has been useful for modeling the carrier and transport properties (conductivity, hall mobility, Seebeck coefficient, and carrier concentration) of many semiconductors.^[41] All of the properties predicted by the effective mass model depend on the position of the Fermi level with respect to the band edge; this includes the bulk carrier concentration, which was measured by blue luminescence in this work. Recent work^[42] has shown that a variant of the standard effective mass model can describe the electronic properties of n-type STO especially well. This model is particularly effective for connecting carrier concentration and Fermi level, because it accounts for the cylindrical topology of STO Fermi surfaces. By contrast, the standard effective mass model assumes that Fermi surfaces are spherical, which is not applicable to STO. The cylindrical variant of the effective mass model has two key parameters: a curvature effective mass and a cylindrical length (constrained by the unit-cell length a of STO, $2\pi/a = 1.6 \text{ \AA}^{-1}$). We use the same curvature mass presented in ref. [42] (1.5 free-electron masses), since this mass successfully described the carrier properties of STO samples with various doping levels. The effective mass and cylindrical length determine the electronic density of states, which along with the Fermi level and temperature (300 K in our experiments), determines the carrier concentration (we reserve the term Fermi energy for the Fermi level at 0 K). Conversely, temperature and carrier concentration can be used to solve for the Fermi level. This model predicts a bulk Fermi level position slightly below the conduction band edge at 300 K and that the Fermi level rises along the length of the oxygen vacancy gradient, due to the rising bulk electron concentration (Figure 5b). It is important to keep in mind that the Fermi–Dirac distribution function is quite broad at 300 K, which explains why the Fermi level is below the conduction band minimum, despite the material being a heavily doped semiconductor.

We can infer the relative positions of the surface and bulk conduction band minima from the core-level XPS binding energy data, in which the shift in core-level binding energy informs the amount of surface band bending. Since the Fermi level is varying along the length of the oxygen vacancy gradient,

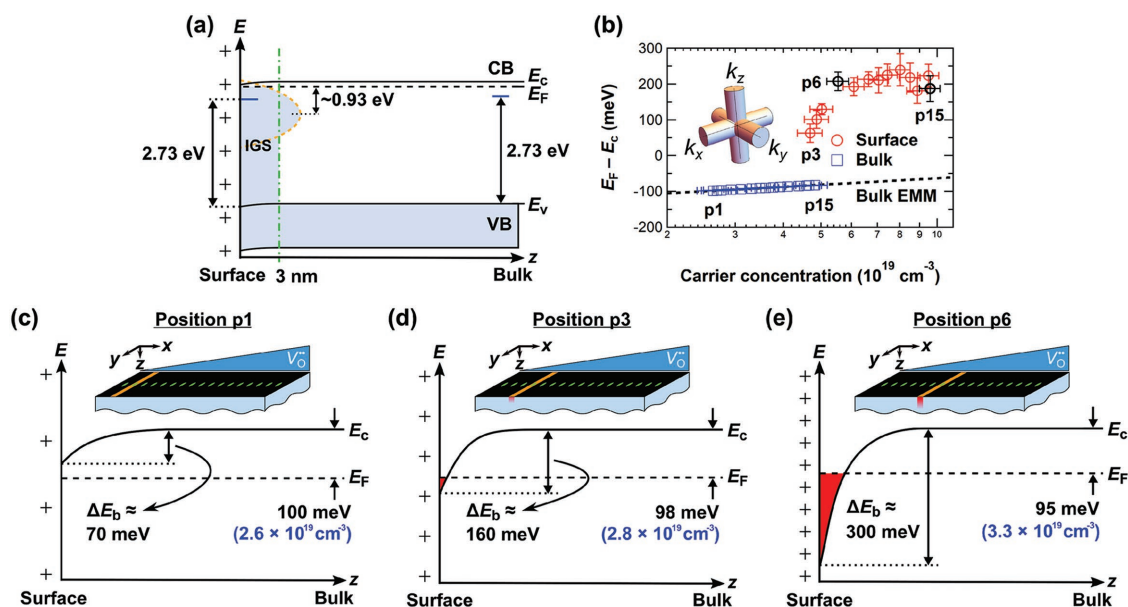


Figure 5. Schematic band diagrams and results of effective mass modeling (EMM) to explain the varying depth distributions of doped electrons (at 300 K) along the length of the oxygen vacancy gradient. a) General band diagram at a given position along the oxygen vacancy gradient. The selvedge region within 3 nm of the surface exhibits downward band bending and gap-states (IGS) induced by oxygen vacancies and TiO_x phases at the surface, including broad Ti 3d-derived states peaked ≈ 0.93 eV below the Fermi level E_F . Deep-level trap states responsible for the blue luminescence are positioned 2.73 eV above the valence band maximum E_v . b) Extracted positions of the Fermi level with respect to the conduction band minimum, $E_F - E_c$, and doped electron concentrations. Results of EMM calculations used for the bulk electrons are also plotted (dashed line), along with a schematic illustration of the bulk Fermi surface used in the model. Surface component data corresponding to positions p6 and p15 are highlighted by black markers. Uncertainties are given by standard deviations. c–e) Band diagrams near the conduction band edge corresponding to positions p1, p3, and p6, respectively. Shown are the Fermi level positions consistent with the bulk doped electron concentrations and estimates of the downward band bending ΔE_b . In-gap states are omitted for clarity.

more detailed depth-dependent band diagrams are presented by Figure 5c–e for positions p1, p3, and p6, along the length of our sample. These positions were chosen to reflect key features in the surface carrier concentrations and band bending data. At positions p1 and p2, the relatively low degree of surface reduction corresponds to relatively small amounts of band bending and electron accumulation near the surface. By position p3, surface band bending has pushed the Fermi level within the conduction bands, corresponding to the position at which we begin to observe a surface carrier concentration with blue luminescence. The surface band bending increases until position p6 (due to the increased concentration of surface oxygen vacancies), where it finally saturates at 300 meV. The only change to the band diagram picture after position p6 is that the Fermi level continues to rise relative to the conduction band minimum.

The band diagrams that we present in Figure 5c–e are consistent with both surface 2DEG bandwidths and electron concentrations reported in the literature (in the saturation region of band bending). From our estimation, 300 meV of band bending with a Fermi level 100 meV below the bulk conduction band minimum indicates the surface 2DEG bandwidth is ≈ 200 meV. Similar saturation of the core-level shifts and 2DEG bandwidths were reported for the quantized states of oxygen vacancy-induced 2DEGs in (001)-oriented STO.^[27,28,31] We note that a similar behavior has been observed in other orientations of STO,^[32] and the seemingly universal band bending behavior merits further investigation. In addition, for a surface electron

accumulation width of 3 nm, the maximum surface sheet carrier density in our STO sample is $\approx 3 \times 10^{13} \text{ cm}^{-2}$. We note that this value is an underestimate, as it does not account for the decaying electron density profile from the surface, which is known to exist for similar 2DEGs formed at the LAO/STO interface.^[43] We further note that while this estimated density is lower than the vacancy-induced surface 2DEG densities around $1 \times 10^{14} \text{ cm}^{-2}$ reported in other works,^[27–29,44] this difference is likely due to the more gradual decay in the oxygen vacancies perpendicular to the surface in our sample. In other STO-based 2DEGs generated by in situ cleaving/UV light irradiation, oxygen vacancies are mainly confined to the surface unit cells. Due to the vacuum annealing method employed in our study, the 2DEG instead exists within a region near the surface which has a gradient of oxygen vacancies perpendicular to the surface, which would correspondingly lower the electric field and hence the electron accumulation.

Application of the bulk effective mass model to the surface carriers nevertheless highlights a key feature of the surface density of states. In Figure 5b, we have used the degree of band bending (measured by XPS) and the fact that the Fermi level must be constant throughout the sample to determine the position of the Fermi level with respect to the surface conduction band minimum ($E_F - E_c$) along the length of the sample. Here, $E_F - E_c$ for the surface states is higher for a given density than predicted by the effective mass model, which indicates that the surface density of states is far lower than the bulk density of states. Other investigations in the

literature reveal that there is likely significant band renormalization occurring simultaneously with the existence of quantum-confined subbands near the STO surface.^[33,45] The work of King et al.^[46] also found that a space-charge potential from oxygen vacancies explains the near-surface band bending observed from ARPES measurements, which supports the theory that quantum confinement changes the nature of the electronic states near the surface of STO. The inconsistency of the bulk effective mass model with the surface data collected in this work offers further proof that quantum confinement shapes the density of states of the surface subbands at both STO surfaces and interfaces.

3. Conclusions

In summary, we systematically characterized the evolving electronic structure and spatial distribution of doped electrons across a gradient of oxygen vacancies formed on a TiO₂-terminated STO (001) single crystal using in situ soft X-ray spectroscopy. The emergence of near-surface electrons obtained from measurements of blue luminescence decays was found to be concomitant with significant surface downward band bending, and was interpreted in terms of 2DEG formation. Effective mass modeling was used to relate the measured electron concentrations near the surface and in the bulk by the position of the Fermi level at each position along the length of the oxygen vacancy gradient. The relation between Fermi levels and carrier concentrations near the surface highlights the lowered (and reconstructed) density of states near the surface due to the quantized nature of the Ti 3d states one would expect from 2DEG formation. Our results indicate that simple vacuum annealing of STO leads to 2DEG formation near the surface, with a density that can be tuned by varying the Fermi level (tied to the bulk carrier concentration) and the degree of surface band bending. The quantitative band-diagram descriptions provided in this work enable precise engineering of the near-surface carrier densities on STO substrates for the fabrication of optimal oxide interfaces.

4. Experimental Section

Sample Preparation and Annealing Process: A DC annealing method was used to prepare a lateral gradient of oxygen vacancies across a STO (001) single crystal inside a UHV chamber at beamline 4-ID-C of the Advanced Photon Source (APS). All subsequent measurements were performed immediately following the annealing process in the same chamber without breaking the vacuum conditions. We adopted the heater setup described in ref. [47] using a 150 nm thick Pt film deposited on the backside of the crystal, schematically illustrated in Figure 1d. Prior to the Pt film deposition, the STO (001) crystal (Crystec) was cut to 10 mm × 4 mm × 1 mm, cleaned with solvents and deionized water, then etched in a buffered hydrofluoride solution (NH₄F:HF = 3:1) of pH 5–5.5 and annealed at 1050 °C for 3 h in 200 sccm flowing O₂ to produce a TiO₂-terminated stepped-and-terraced surface with 0.4 nm height steps (see inset atomic force microscopy image in Figure 1d). The DC field was varied to achieve a temperature ramp rate of $\approx \pm 20$ °C min⁻¹. During the annealing process, the chamber pressure ranged between 5×10^{-10} and 6×10^{-9} Torr and the sample region near the cathode was hottest at 800 °C, while the region near the anode was cooler at 700 °C, where

the temperature was measured using an infrared pyrometer with the emissivity set to 0.70.

Soft X-Ray Spectroscopy: Soft X-ray spectroscopy measurements were performed without breaking vacuum conditions in the same UHV chamber following the annealing processes. Spatially dependent measurements were made along the oxygen vacancy gradient in 0.38 mm steps using X-rays focused to $\approx 350 \mu\text{m} \times 150 \mu\text{m}$ spot size at normal incidence.

Time-resolved XEOL spectroscopy measurements were performed using 1350 eV pulsed (153 ns separation, 33 ps pulse width) X-rays with 45° incidence and 30° emission angles with respect to the sample surface, where the luminescence spectra were collected by a photomultiplier tube equipped with a monochromator. The depth sensitivity is given by the sample-dependent X-ray penetration length (PL), which we define as the distance into the sample at which the X-ray intensity decays to 1/e of the intensity at the surface for a particular incident angle. Under our XEOL measurement conditions, the PL for the STO sample was 706 nm.^[48] The XEOL decay curves were measured by collecting the photons emitted with 2.73 eV energy using methods described previously in ref. [49]. Prior to these measurements, the instrument response function (IRF) for the measurement setup was obtained by measuring the decay of the bandgap exciton peak (3.4 eV) of a GaN film, which has a lifetime shorter than the time resolution of the photomultiplier tube.

XPS measurements were taken using X-rays with 1000 eV energy at varying emission angles (measured with respect to the sample surface) using an Omnicron Argus electron energy analyzer. The binding energy scales for all XPS measurements were calibrated by setting the Au 4f_{7/2} peak to 84.0 eV, where the gold foil was placed in electrical contact with the sample surface. No charging was observed on the STO sample after the annealing process.

XAS measurements were taken simultaneously in total electron yield (TEY) and Auger electron yield (AEY) modes. TEY-mode XAS measurements were performed by measuring the sample restoring current from the electrons ejected by the absorption process, which nominally gives a probe depth of 5–10 nm in oxides.^[50] AEY-mode XAS measurements were performed by collecting the Ti LMM Auger electrons with 381 eV kinetic energy at 80° emission angle, which gives a 95% probe depth of 1.6 nm in STO. Normalization was performed by measuring the restoring current of an in situ coated gold mesh inserted into the X-ray beam. RESPES of the valence band region were taken following a Ti L-edge XAS measurement to choose the photon energies of interest, where the binding energy scales were again referenced with respect to the Au 4f_{7/2} peak set to 84.0 eV. The emission angle for the RESPES measurements was fixed to 80°, which gave a 95% probe depth of ≈ 5 nm for the incident X-ray energies between 450.0 and 460.5 eV.

Supporting Information

Supporting Information is available from the Wiley Online Library or from the author.

Acknowledgements

Work by S.C. and D.D.F. was supported by the U.S. Department of Energy (DOE), Office of Science, Basic Energy Sciences (BES), Materials Science Division. Use of the Advanced Photon Source was supported by the DOE, Office of Science, BES, under Contract No. DE-AC02-06CH11357. Work by M.T.D. and G.J.S. was supported by the National Science Foundation (NSF), Division of Materials Research (DMR) under Grant Nos. 1334713 and 1333335. Work by Z.R.M. was supported by the DOE (DE-FG02-03ER15457) through the Institute for Catalysis in Energy Processes at Northwestern University. Work by L.D.M. was supported by the DOE, Office of Science, BES, under Award No. DE-FG02-01ER45945.

Conflict of Interest

The authors declare no conflict of interest.

Keywords

effective mass modeling, electronic structure, in-situ x-ray spectroscopy, oxygen vacancies, SrTiO₃ surface

Received: July 21, 2018

Revised: September 17, 2018

Published online:

- [1] N. Reyren, S. Thiel, A. D. Caviglia, L. F. Kourkoutis, G. Hammerl, C. Richter, C. W. Schneider, T. Kopp, A.-S. Rüetschi, D. Jaccard, M. Gabay, D. A. Muller, J.-M. Triscone, J. Mannhart, *Science* **2007**, 317, 1196.
- [2] H. Y. Hwang, Y. Iwasa, M. Kawasaki, B. Keimer, N. Nagaosa, Y. Tokura, *Nat. Mater.* **2012**, 11, 103.
- [3] J. Mannhart, D. G. Schlom, *Science* **2010**, 327, 1607.
- [4] A. Ohtomo, H. Y. Hwang, *Nature* **2004**, 427, 423.
- [5] Y. Chen, N. Pryds, J. E. Kleibecker, G. Koster, J. Sun, E. Stamate, B. Shen, G. Rijnders, S. Linderth, *Nano Lett.* **2011**, 11, 3774.
- [6] G. Herranz, F. Sánchez, N. Dix, M. Scigaj, J. Fontcuberta, *Sci. Rep.* **2012**, 2, 758.
- [7] P. Moetakef, J. Y. Zhang, A. Kozhanov, B. Jalan, R. Seshadri, S. J. Allen, S. Stemmer, *Appl. Phys. Lett.* **2011**, 98, 112110.
- [8] Y. Z. Chen, N. Bovet, F. Trier, D. V. Christensen, F. M. Qu, N. H. Andersen, T. Kasama, W. Zhang, R. Giraud, J. Dufouleur, T. S. Jespersen, J. R. Sun, A. Smith, J. Nygård, L. Lu, B. Büchner, B. G. Shen, S. Linderth, N. Pryds, *Nat. Commun.* **2013**, 4, 1371.
- [9] Z. Q. Liu, C. J. Li, W. M. Lü, X. H. Huang, Z. Huang, S. W. Zeng, X. P. Qiu, L. S. Huang, A. Annadi, J. S. Chen, J. M. D. Coey, T. Venkatesan, Ariando, *Phys. Rev. X* **2013**, 3, 021010.
- [10] S. Thiel, G. Hammerl, A. Schmehl, C. W. Schneider, J. Mannhart, *Science* **2006**, 313, 1942.
- [11] C. Cen, S. Thiel, G. Hammerl, C. W. Schneider, K. E. Andersen, C. S. Hellberg, J. Mannhart, J. Levy, *Nat. Mater.* **2008**, 7, 298.
- [12] A. D. Caviglia, S. Gariglio, N. Reyren, D. Jaccard, T. Schneider, M. Gabay, S. Thiel, G. Hammerl, J. Mannhart, J.-M. Triscone, *Nature* **2008**, 456, 624.
- [13] M. Ben Shalom, M. Sachs, D. Rakhmievitch, A. Palevski, Y. Dagan, *Phys. Rev. Lett.* **2010**, 104, 126802.
- [14] C. Richter, H. Boschker, W. Dietsche, E. Fillis-Tsirakis, R. Jany, F. Loder, L. F. Kourkoutis, D. A. Muller, J. R. Kirtley, C. W. Schneider, J. Mannhart, *Nature* **2013**, 502, 528.
- [15] L. Li, C. Richter, J. Mannhart, R. C. Ashoori, *Nat. Phys.* **2011**, 7, 762.
- [16] A. D. Caviglia, M. Gabay, S. Gariglio, N. Reyren, C. Cancellieri, J.-M. Triscone, *Phys. Rev. Lett.* **2010**, 104, 126803.
- [17] A. Fête, S. Gariglio, C. Berthod, D. Li, D. Stornaiuolo, M. Gabay, J.-M. Triscone, *New J. Phys.* **2014**, 16, 112002.
- [18] S. Hurand, A. Jouan, C. Feuillet-Palma, G. Singh, J. Biscaras, E. Lesne, N. Reyren, A. Barthélémy, M. Bibes, J. E. Villegas, C. Ulysse, X. Lafosse, M. Pannetier-Lecoeur, S. Caprara, M. Grilli, J. Lesueur, N. Bergeal, *Sci. Rep.* **2015**, 5, 12751.
- [19] K. Shin-Ik, K. Dai-Hong, K. Yoonjung, M. S. Young, K. Min-Gyu, C. J. Kwon, J. H. Won, K. S. Keun, C. Ji-Won, Y. Seok-Jin, C. H. Jung, K. Chong-Yun, L. Suyoun, H. Seong-Hyeon, K. Jin-Sang, B. Seung-Hyub, *Adv. Mater.* **2013**, 25, 4612.
- [20] N. Nakagawa, H. Y. Hwang, D. A. Muller, *Nat. Mater.* **2006**, 5, 204.
- [21] A. Kalabukhov, R. Gunnarsson, J. Börjesson, E. Olsson, T. Claeson, D. Winkler, *Phys. Rev. B* **2007**, 75, 121404.
- [22] G. Herranz, M. Basletić, M. Bibes, C. Carrétéro, E. Tafrá, E. Jacquet, K. Bouzehouane, C. Deranlot, A. Hamzić, J.-M. Broto, A. Barthélémy, A. Fert, *Phys. Rev. Lett.* **2007**, 98, 216803.
- [23] W. Siemons, G. Koster, H. Yamamoto, W. A. Harrison, G. Lucovsky, T. H. Geballe, D. H. A. Blank, M. R. Beasley, *Phys. Rev. Lett.* **2007**, 98, 196802.
- [24] M. Basletic, J.-L. Maurice, C. Carrétéro, G. Herranz, O. Copie, M. Bibes, É. Jacquet, K. Bouzehouane, S. Fusil, A. Barthélémy, *Nat. Mater.* **2008**, 7, 621.
- [25] L. Qiao, T. C. Droubay, T. Varga, M. E. Bowden, V. Shutthanandan, Z. Zhu, T. C. Kaspar, S. A. Chambers, *Phys. Rev. B* **2011**, 83, 085408.
- [26] L. Yu, A. Zunger, *Nat. Commun.* **2014**, 5, 5118.
- [27] W. Meevasana, P. D. C. King, R. H. He, S.-K. Mo, M. Hashimoto, A. Tamai, P. Songsirithigul, F. Baumberger, Z.-X. Shen, *Nat. Mater.* **2011**, 10, 114.
- [28] A. F. Santander-Syro, O. Copie, T. Kondo, F. Fortuna, S. Pailhes, R. Weht, X. G. Qiu, F. Bertran, A. Nicolaou, A. Taleb-Ibrahimi, P. Le Fevre, G. Herranz, M. Bibes, N. Reyren, Y. Apert, P. Lecoeur, A. Barthelemy, M. J. Rozenberg, *Nature* **2011**, 469, 189.
- [29] S. M. Walker, F. Y. Bruno, Z. Wang, A. de la Torre, S. Riccò, A. Tamai, T. K. Kim, M. Hoesch, M. Shi, M. S. Bahrany, P. D. C. King, F. Baumberger, *Adv. Mater.* **2015**, 27, 3894.
- [30] Z. Wang, S. McKeown Walker, A. Tamai, Y. Wang, Z. Ristic, F. Y. Bruno, A. de la Torre, S. Riccò, N. C. Plumb, M. Shi, P. Hlawenka, J. Sánchez-Barriga, A. Varykhalov, T. K. Kim, M. Hoesch, P. D. C. King, W. Meevasana, U. Diebold, J. Mesot, B. Moritz, T. P. Devereaux, M. Radovic, F. Baumberger, *Nat. Mater.* **2016**, 15, 835.
- [31] N. C. Plumb, M. Salluzzo, E. Razzoli, M. Månsson, M. Falub, J. Krempasky, C. E. Matt, J. Chang, M. Schulte, J. Braun, H. Ebert, J. Minár, B. Delley, K.-J. Zhou, T. Schmitt, M. Shi, J. Mesot, L. Patthey, M. Radović, *Phys. Rev. Lett.* **2014**, 113, 086801.
- [32] L. Dudy, M. Sing, P. Scheiderer, J. D. Denlinger, P. Schütz, J. Gabel, M. Buchwald, C. Schlueter, T.-L. Lee, R. Claessen, *Adv. Mater.* **2016**, 28, 7443.
- [33] T. C. Rödel, C. Bareille, F. Fortuna, C. Baumier, F. Bertran, P. Le Fèvre, M. Gabay, O. Hijano Cubelos, M. J. Rozenberg, T. Maroutian, P. Lecoeur, A. F. Santander-Syro, *Phys. Rev. Appl.* **2014**, 1, 051002.
- [34] D. Kan, T. Terashima, R. Kanda, A. Masuno, K. Tanaka, S. Chu, H. Kan, A. Ishizumi, Y. Kanemitsu, Y. Shimakawa, M. Takano, *Nat. Mater.* **2005**, 4, 816.
- [35] D. Kan, R. Kanda, Y. Kanemitsu, Y. Shimakawa, M. Takano, T. Terashima, A. Ishizumi, *Appl. Phys. Lett.* **2006**, 88, 191916.
- [36] A. Janotti, J. B. Varley, M. Choi, C. G. Van de Walle, *Phys. Rev. B* **2014**, 90, 085202.
- [37] H. Yasuda, Y. Kanemitsu, *Phys. Rev. B* **2008**, 77, 193202.
- [38] Y. Yamada, H. Yasuda, T. Tayagaki, Y. Kanemitsu, *Phys. Rev. Lett.* **2009**, 102, 247401.
- [39] H. Yasuda, Y. Yamada, T. Tayagaki, Y. Kanemitsu, *Phys. Rev. B* **2008**, 78, 233202.
- [40] Y. Aiura, I. Hase, H. Bando, T. Yasue, T. Saitoh, D. Dessau, *Surf. Sci.* **2002**, 515, 61.
- [41] A. F. May, G. J. Snyder, in *Thermoelectrics and Its Energy Harvesting* (Ed: D. M. Rowe), Vol. 1, CRC Press, Boca Raton, FL, USA **2012**, Ch. 11.
- [42] M. T. Dylla, S. D. Kang, G. J. Snyder, in preparation.
- [43] Y. Yamada, H. K. Sato, Y. Hikita, H. Y. Hwang, Y. Kanemitsu, *Appl. Phys. Lett.* **2014**, 104, 151907.
- [44] S. Soltani, S. Cho, H. Ryu, G. Han, B. Kim, D. Song, T. K. Kim, M. Hoesch, C. Kim, *Phys. Rev. B* **2017**, 95, 125103.
- [45] M. Breitschaft, V. Tinkl, N. Pavlenko, S. Paetel, C. Richter, J. R. Kirtley, Y. C. Liao, G. Hammerl, V. Eyert, T. Kopp, J. Mannhart, *Phys. Rev. B* **2010**, 81, 153414.

- [46] P. D. C. King, S. McKeown Walker, A. Tamai, A. de la Torre, T. Eknapakul, P. Buaphet, S.-K. Mo, W. Meevasana, M. S. Bahramy, F. Baumberger, *Nat. Commun.* **2014**, *5*, 3414.
- [47] R. Shimizu, K. Iwaya, T. Ohsawa, S. Shiraki, T. Hasegawa, T. Hashizume, T. Hitosugi, *Appl. Phys. Lett.* **2012**, *100*, 263106.
- [48] B. L. Henke, E. M. Gullikson, J. C. Davis, *At. Data Nucl. Data Tables* **1993**, *54*, 181.
- [49] T.-K. Sham, R. A. Rosenberg, *ChemPhysChem* **2007**, *8*, 2557.
- [50] M. Abbate, J. B. Goedkoop, F. M. F. de Groot, M. Grioni, J. C. Fuggle, S. Hofmann, H. Petersen, M. Sacchi, *Surf. Interface Anal.* **1992**, *18*, 65.